scientific reports

OPEN

First-principles based simulations of electronic transmission in ReS$_2$/WSe$_2$ and ReS$_2$/MoSe$_2$ type-II vdW heterointerfaces

Dipankar Saha[1,2] & Saurabh Lodha[1]

Electronic transmission in monolayer ReS$_2$ and ReS$_2$ based van der Waals (vdW) heterointerfaces are studied here. Since ReS$_2$/WSe$_2$ and ReS$_2$/MoSe$_2$ type-II vdW heterostructures are suitable for near infrared (NIR)/short-wave infrared (SWIR) photodetection, the role of interlayer coupling at the heterointerfaces is examined in this work. Besides, a detailed theoretical study is presented employing density functional theory (DFT) and nonequilibrium Green's function (NEGF) combination to analyse the transmission spectra of the two-port devices with ReS$_2$/WSe$_2$ and ReS$_2$/MoSe$_2$ channels and compare the near-equilibrium conductance values. Single layer distorted 1T ReS$_2$ exhibits formation of parallel chains of 'Re'-'Re' bonds, leading to in-plane anisotropy. Owing to this structural anisotropy, the charge carrier transport is very much orientation dependent in ReS$_2$. Therefore, this work is further extended to investigate the role of clusterized 'Re' atoms in electronic transmission.

In recent years significant progress in micro and nano photonics has been observed owing to the optoelectronic devices based on atomically thin two-dimensional (2D) layered materials and their vertical stacks[1–14]. Such 2D materials can be metallic (graphene) or, semiconducting (e.g., black phosphorus, transition metal dichalcogenides, etc.) or, a combination of both[15–19]. The vdW heterointerfaces formed with vertical stacking of 2D materials may exhibit compelling new properties which are significantly different from those of the participant materials[8,20,21]. Strong interlayer coupling and fast charge transfer across vdW interface are the key features which largely determine performance efficiency of the heterostructures[8,9,20,22,23]. In oder to design ultrafast NIR and SWIR photodetectors, a theoretical study exploring various possible combinations of group-6 and group-7 monolayer transition metal dichalcogenides (TMDs) is presented in[20]. The detection and visualization of NIR/SWIR are crucial to successful design and implementation of various biomedical devices, sensors, and cameras for surveillance[24,25]. Type-II heterointerfaces are necessary for those applications. As the conduction band minimum and valence band maximum reside in different layers, a type-II heterointerface can offer efficient e$^-$ and h$^+$ separation at the junction[20,26,27]. Among different combinations of type-II vdW heterostructures, it has been found that both ReS$_2$/WSe$_2$ and ReS$_2$/MoSe$_2$ emerge as suitable candidates with efficient generation, separation, and collection of charge carriers[20]. Howbeit, the effects of interlayer coupling on the electronic structures of ReS$_2$/WSe$_2$ and ReS$_2$/MoSe$_2$ were not captured in[20]. Moreover, to quantify the near-equilibrium conductance values of those heterointerfaces, a detailed analysis of electronic transmission through the ReS$_2$/WSe$_2$ and the ReS$_2$/MoSe$_2$ needs to be conducted.

Thus, in this work, considering band dispersions and electron difference density (EDD) calculations, first we try to investigate the role of interlayer coupling at the vdW heterojunctions. Next, utilizing NEGF along with DFT, we have shown the electronic transmission of two-port devices with the ReS$_2$/WSe$_2$ and the ReS$_2$/MoSe$_2$ channels and compared their conductance values at near-equilibrium.

Besides, we have also investigated the anisotropic carrier transmission of the group-7 constituent material, that is distorted 1T ReS$_2$. But for the group-6 TMDs (e.g., MoS$_2$, WS$_2$, MoSe$_2$, and WSe$_2$), because of the symmetric honeycomb structure of semiconducting 2H phase, such in-plane anisotropy is generally not expected[20,28]. Furthermore, it is worth mentioning that orientation dependent electro-thermal transport in 2D layered materials can be useful for the purpose of designing low power, ultrathin next generation electronic devices[28–33]. Among various 2D materials, in-plane anisotropy owing to structural transformation is seen in the 1T′ phase of the

[1]Department of Electrical Engineering, Indian Institute of Technology Bombay, Mumbai 400076, India. [2]Department of Electronics and Telecommunication Engineering, Indian Institute of Engineering Science and Technology Shibpur, Howrah 711103, India. ✉email: dipsah_etc@yahoo.co.in

MoS_2[28,34]. Strong anisotropic conductance, due to clusterization of 'Mo' atoms along the transport direction, is reported in[28]. A similar trend can be seen in distorted 1T ReS_2, where the formation of parallel chains of 'Re'-'Re' bonds can lead to orientation dependent anisotropic transport[29]. As reported in[29], distorted 1T ReS_2 exhibits direction dependent I-V as well as transfer characteristics. Such experimental observation motivated us to explore the electronic properties of single layer distorted 1T ReS_2 and investigate the role of clusterized 'Re' atoms in carrier transmission.

Methodology

In order to coduct first-principles based DFT calculations, the software package "QuantumATK" was used[35,36]. For all the unit cells and the supercells, computation of electronic structures and geometry optimizations were performed using the generalized gradient approximation (GGA) as exchange correlation along with the Perdew-Burke-Ernzerhof (PBE) functional[37]. Moreover, LCAO (linear combination of atomic orbitals) based numerical basis sets were utilized in this study to obtain results at the cost of reasonable computational load[28,35]. To attain good accuracy of quantum transport and electronic structure calculations, the OPENMX (Open source package for Material eXplorer) code was used as the norm-conserving pseudopotentials[38,39]. The basis sets for Mo, S, W, Se, and Re were taken as "s3p2d1", "s2p2d1", "s3p2d1", "s2p2d1", and "s3p2d1" respectively. Besides, the density mesh cut-off value was set to 200 Hartree and the k-points in Monkhorst-Pack grid were set to 9×9×1 (X-Y-Z) for the unit cells and 9×9×3 for the heterostructures. Sufficient vacuum was incorporated along the direction normal to the in-plane for the purpose of avoiding spurious interaction between periodic images. Furthermore, to include the effects of vdW interactions among different monolayers, the Grimme's dispersion correction (DFTD2) was employed[40]. The DFTD2 scheme can provide accurate results with medium to large interatomic distances, like other van der Waals density functionals[20,41].

Considering the two-port devices, transmission spectra along the channels were computed utilizing NEGF along with DFT. The k-points in Monkhorst-Pack grid were adopted as 1×9×150 for the device calculations. Apart from that, in order to solve the Poisson's equation, Dirichlet boundary condition in the transport direction (Z direction) and periodic boundary conditions in the other two directions (X–Y directions) were assigned. In the framework of NEGF, taking into account the broadening matrices $\Gamma_{l,r}(E) = i[\Sigma_{l,r} - \Sigma_{l,r}^{\dagger}]$ for the left and the right electrodes (set by computing the self energy matrices Σ_l and Σ_r)[42,43], the electronic transmission can be calculated as,

$$T_e(E) = \text{Tr}[\Gamma_l(E)\,G(E)\,\Gamma_r(E)\,G^{\dagger}(E)]\,, \qquad (1)$$

where $G(E)$ and $G^{\dagger}(E)$ denote retarded Green's function and advanced Green's function respectively[28,42,44]. Moreover, utilizing the concept of linear coherent transport, the conductance due to charge carriers and the Seebeck coefficient can be calculated as[36,42,43],

$$G_e(\mu) = q^2 \times L_{f,0}, \qquad (2)$$

and

$$S = \frac{1}{qT} \times \frac{L_{f,1}}{L_{f,0}}. \qquad (3)$$

Considering the Fermi distribution function f(μ, E), the following expression can be used to determine $L_{f,0}$ and $L_{f,1}$[42,43].

$$L_{f,n}(\mu) = \frac{2}{h} \times \int_{-\infty}^{+\infty} T_e(E)\,(E-\mu)^n \left(\frac{-\partial f(\mu, E)}{\partial E}\right) dE \qquad (4)$$

Results and discussion

Figure 1 illustrates a typical type-II vdW heterostructure formed with vertical stacking of group-6 and group-7 monolayer TMDs, as well as highlights its salient features[20]. Considering NIR/SWIR photodetection, near-direct bandgap, larger band offset values, and feasibility of integrating with flexible substrates make monolayer ReS_2 (group-7 TMD)/ monolayer WSe_2 (group-6 TMD) heterointerface a potentially promising candidate for the next generation ultrathin optoelectronic device[2,9,17,20]. Even with the increase in number of layers of ReS_2 and WSe_2, we find that the near-direct type-II band alignment remains unaltered, hence ensuring efficient optical generation across the vdW interface[22]. Apart from that, monolayer ReS_2 (group-7 TMD)/ monolayer $MoSe_2$ (group-6 TMD) heterostructure can also be suitable for NIR/SWIR photodetection owing to its near-direct bandgap and superior optical absorption of the constituent $MoSe_2$ layer[20].

Figures 2 and 3 depict the electronic structures of ReS_2/WSe_2 and $ReS_2/MoSe_2$ considering element-wise contributions[45–47]. Both the projected density of states (DOS) plots exhibit type-II band alignments with energy gap values of 0.684 eV and 0.842 eV for the ReS_2/WSe_2 and the $ReS_2/MoSe_2$ heterostructures.

Besides, the in-plane lattice constants and the equilibrium interlayer distance for the hexagonal vdW heterointerface of ReS_2/WSe_2 (Fig.2 inset) are a = b = 6.600 Å and 3.49 Å respectively[20]. Those values for $ReS_2/MoSe_2$ interface (Fig. 3 inset) are a = b = 6.597 Å and 3.41 Å[20].

In order to determine the effect of interlayer coupling, next we carry out a detailed analysis which emphasizes mainly on the band dispersions and the electron difference density (EDD) calculations of the heterointerfaces[48]. We consider the equilibrium interlayer distances of ReS_2/WSe_2 and $ReS_2/MoSe_2$ as the references. Those equilibrium distances along with the in-plane lattice constants are computed while optimizing the geometries utilizing
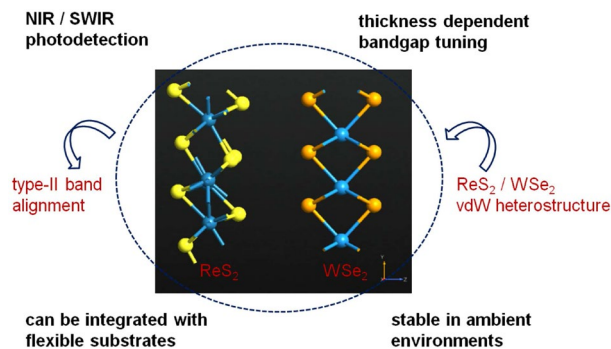
**Figure 1.** Vertical stacking of group-6 and group-7 monolayer TMDs to form a type-II vdW heterointerface (viz. ReS_2/WSe_2).
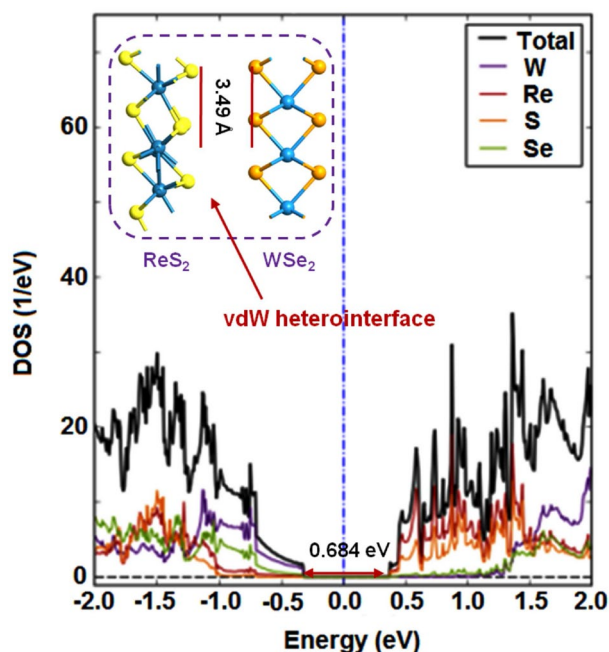
Figure 2. Projected DOS plots for ReS_2/WSe_2 vdW heterointerface.

LBFGS (Limited-memory Broyden Fletcher Goldfarb Shanno) algorithm with force tolerance of 0.01 eV/Å and stress tolerance of 0.001 eV/Å^3. We also maintain the stacking patterns of the fully relaxed heterostructures same as those obtained form geometry optimization calculations. We then vary the interlayer distances (d_{int}), and compute band dispersions of the vdW heterostructures (Fig. S1a and S1b). The changes in indirect and direct bandgap (I_{gap} and D_{gap}) values, as we deviate from the equilibrium interlayer distances, are listed in Table 1.

I_{gap} and D_{gap} for ReS_2/WSe_2 are 0.68 eV and 0.83 eV, when the d_{int} is 3.49 Å (equilibrium interlayer distance). On the other hand, I_{gap} and D_{gap} for $ReS_2/MoSe_2$ are 0.84 eV and 0.98 eV, when the d_{int} is 3.41 Å (equilibrium interlayer distance). Now, as we shift the d_{int} around the equilibrium distances, we find that there are no noteworthy changes in band dispersions of ReS_2/WSe_2 and $ReS_2/MoSe_2$ (Fig. S1a and S1b), though the I_{gap} and the D_{gap} values do vary. We denote these changes as $\Delta E_I|$ and $\Delta E_D|$ (Table 1). Moreover, it is important to note that the variations in $\Delta E_I|$ and $\Delta E_D|$ are similar for the aforementioned type-II heterostructures.

Hence, we look into another important aspect, that is the EDD or the charge re-distribution between the constituent layers. As depicted in the cut plane diagrams of Fig. 4, negative and positive values of EDD indicate charge depletion and charge accumulation respectively. The EDD plot for ReS_2/WSe_2 (Fig. 4a) delineates minimum and maximum values of difference density as -0.29 and 0.2 Å^{-3}. Thus the corresponding average value is $\sim$ -0.04 Å^{-3}. On the other hand, EDD plot for $ReS_2/MoSe_2$ (Fig. 4b) shows minimum and maximum values of difference density as -0.29 and 0.79 Å^{-3}, with the average of $\sim$ 0.25 Å^{-3}. The larger average value of EDD for the $ReS_2/MoSe_2$ interface is essentially interpreting more charge distribution. Therefore, we can expect much stronger effect of interlayer coupling at the heterointerface of $ReS_2/MoSe_2$. Apart from that, the binding energy value of -0.403 eV ensures better energetic stability of $ReS_2/MoSe_2$ compared to that of ReS_2/WSe_2 (− 0.310
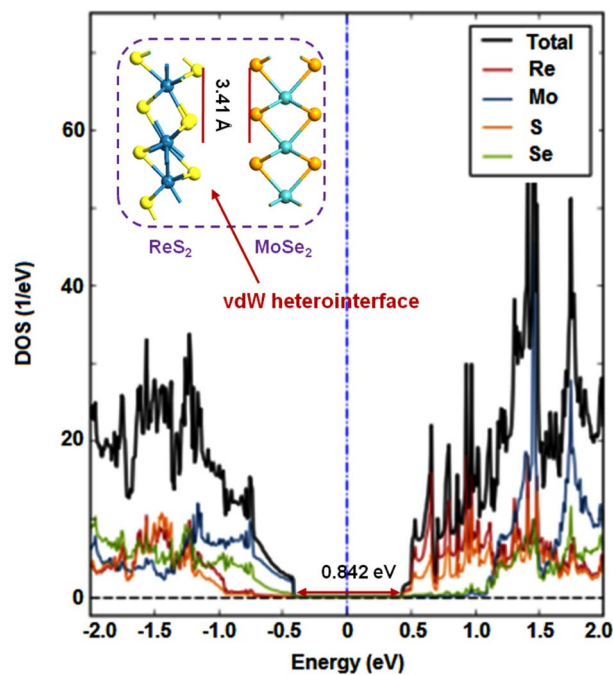
**Figure 3.** Projected DOS plots for ReS_2/$MoSe_2$ vdW heterointerface.

Interface	d_{int} (Å)	I_{gap} (eV)	D_{gap} (eV)	$|\Delta E_I|$ (eV)	$|\Delta E_D|$ (eV)
ReS_2/WSe_2	2.69	0.80	0.89	0.12	0.06
	3.49	0.68	0.83	0.00	0.00
	4.30	0.66	0.83	0.02	0.00
	5.10	0.66	0.82	0.02	0.01
ReS_2/$MoSe_2$	2.71	0.92	0.96	0.08	0.02
	3.41	0.84	0.98	0.00	0.00
	4.48	0.82	0.98	0.02	0.00
	5.18	0.81	0.97	0.03	0.01

**Table 1.** Change in bandgap with the varying interlayer distances.

eV)[20]. In the following, we have further compared the electronic transmission in both the vdW heterointerfaces and observed a similar trend. At steady state, considering the two-port devices, the electron density in channel can be calculated as n_{ch} (r) = n_{left} (r) + n_b (r) + n_{right} (r), where n_{left} (r), n_{right} (r), and n_b (r) are the contributions from the extended left electrode, the extended right electrode, and the bound states[36]. The electrostatic potential as well as electron density of the central region will depend on occupation of bound states[36]. Therefore, strong interlayer coupling via charge re-distribution at the heterointerface can play significant role in determining the charge carrier transport[27,36].

Next, to model the two-port devices, we take into account the geometry optimized vertical stacks of ReS_2/WSe_2 and ReS_2/$MoSe_2$ as illustrated in Figs. 2 and 3 (insets). As shown in Fig. 5, the group-7 and the group-6 TMD layers are extended to form the left and the right electrodes respectively. For the ReS_2/WSe_2 device, t_{left} (length of the left electrode) = t_{right} (length of the right electrode) is ∼ 6.60 Å. For the ReS_2/$MoSe_2$ device, that value is ∼ 6.59 Å. The length and the width of the channel region of ReS_2/WSe_2 two-port device are 6.658 nm and 1.143 nm (Fig. 5a). Considering the channel region of ReS_2/$MoSe_2$ two-port device, those values are 6.654 nm and 1.142 nm respectively (Fig. 5b). Besides, for those composite two-port device structures, the overlapping regions are maintained as ∼ 2.423 nm. It is worth mentioning that the mean absolute strain values on both the monolayer surfaces are 0.61% and 0.59% for ReS_2/WSe_2 and ReS_2/$MoSe_2$ channels[20].

Figure 6 shows the transmission spectra (zero bias) of the two-port devices, where we can observe that the transmission through ReS_2/$MoSe_2$ channel is slightly better than that in ReS_2/WSe_2 (cosidering a small energy range near the energy zero level). In order to quantify this we further calculate the near-equilibrium conductance and Seebeck coefficient values, as listed in Table 2. As discussed previously, S and G_e denote the Seebeck coefficient and the electrical conductance, computed utilizing the linear response approximation (∼ 300 K)[28,43]. ΔE_F represents the shift in energy level from the energy zero. Moreover, the plots of Seebeck coefficients for
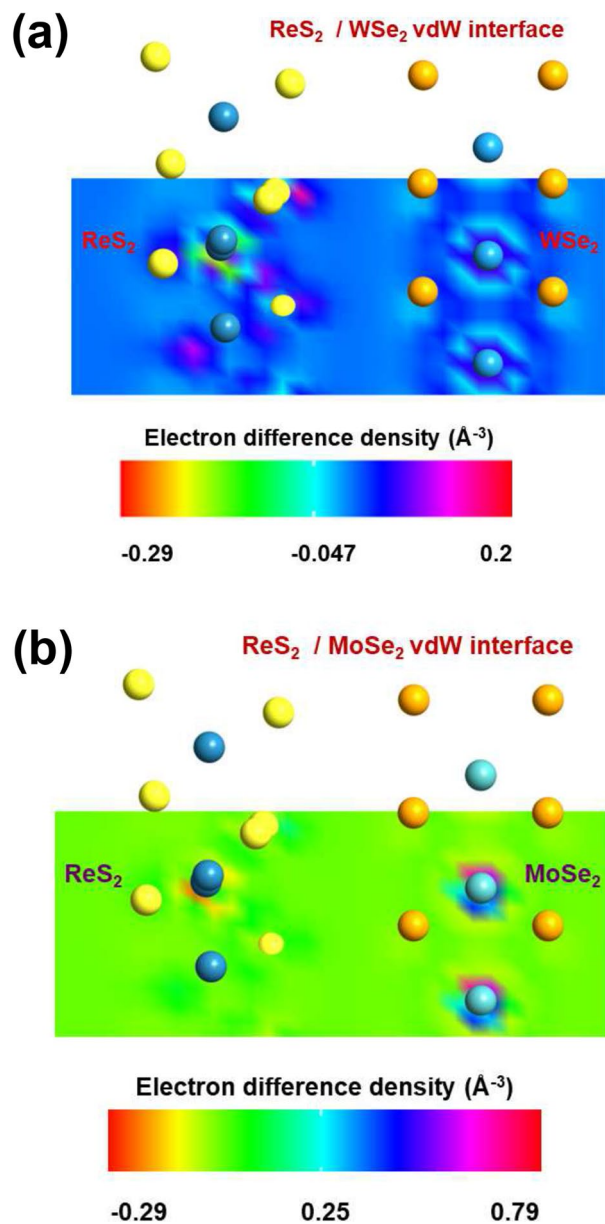
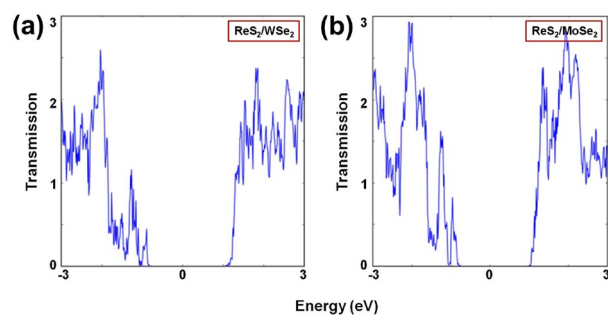**Figure 4.** EDD plots showing charge re-distribution between the constituent layers of (**a**) ReS_2/WSe_2 and (**b**) ReS_2/$MoSe_2$.
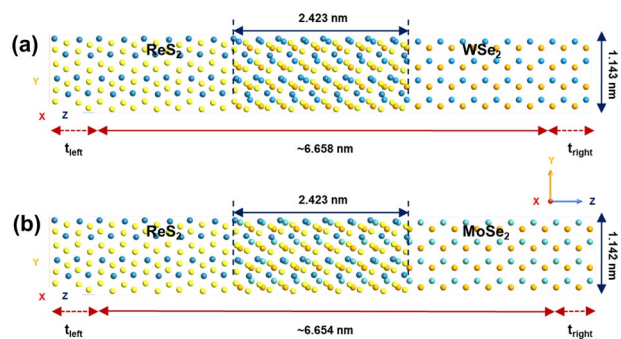
**Figure 5.** Atomistic models of the two-port devices with (**a**) ReS_2/WSe_2 and (**b**) ReS_2/$MoSe_2$ channels.

Figure 6. Transmission spectra of the two-port devices with (**a**) ReS_2/WSe_2 and (**b**) $ReS_2/MoSe_2$ channels.

Two-port devices	ΔE_F (eV)	G_e (S)	S (V/K)
ReS₂/WSe₂ (length = 6.658 nm width = 1.143 nm)	0.9	2.906×10^{-9}	-0.0004686
	1.0	9.022×10^{-8}	-0.0002988
	1.1	1.023×10^{-6}	-0.0001835
	1.2	8.563×10^{-6}	-0.0001511
	1.3	3.540×10^{-5}	-4.829×10^{-5}
	1.4	5.180×10^{-5}	-1.856×10^{-5}
	1.8	7.897×10^{-5}	-9.423×10^{-6}
ReS₂/MoSe₂ (length = 6.654 nm width = 1.142 nm)	0.9	4.925×10^{-8}	-0.0004324
	1.0	1.396×10^{-6}	-0.0002594
	1.1	1.252×10^{-5}	-0.000103
	1.2	3.497×10^{-5}	-5.931×10^{-5}
	1.3	6.848×10^{-5}	-2.906×10^{-5}
	1.4	7.434×10^{-5}	-1.313×10^{-5}
	1.8	8.396×10^{-5}	-1.164×10^{-5}

**Table 2.** Details of near-equilibrium conductance values.
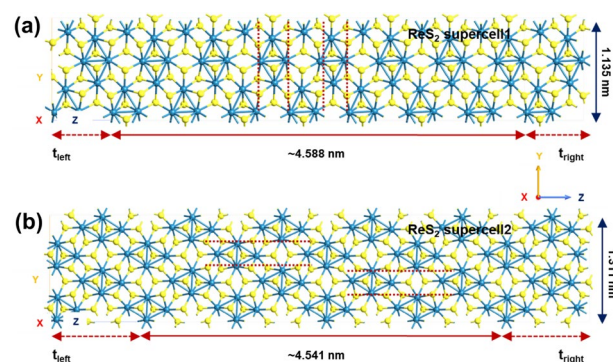
Figure 7. Atomistic models of (**a**) ReS_2 supercell1 and (**b**) ReS_2 supercell2, obtained by keeping the 'Re'-'Re' bonds are either perpendicular or parallel to the transport direction.

the energy range of -3–3 eV are shown in Fig. S2. Similar to the trends of transmission spectra (Fig. 6), the G_e values listed Table 2 reinforce that the $ReS_2/MoSe_2$ channel is more conducive to the charge carrier transport.

Next, we have extended this theoretical study to demonstrate in-plane anisotropy and orientation dependent carrier transmission in single layer distorted 1T ReS_2. For the purpose of modeling the two-port devices with distorted 1T ReS_2 channels, we consider three different supercells viz. 'ReS_2 supercell1' (where the diamond-shaped DS 'Re' chains are perpendicular to the transport direction), 'ReS_2 supercell2' (where the DS 'Re' chains are parallel to the transport direction), and 'ReS_2 supercell3' (where the structure is obtained from the geometry optimized ReS_2/WSe_2 and the angle between a_1-b_1 and b_1-c_1 is $\sim 123°$)[20,29].

Figure 7 shows the atomistic models of the two-port devices with 'ReS_2 supercell1' (length = 4.588 nm and width = 1.135 nm) and 'ReS_2 supercell2' (length = 4.541 nm and width = 1.311 nm) channel regions. Figures 8 and 9 illustrate the electron density plots and zero bias transmission spectra of 'ReS_2 supercell1' and 'ReS_2
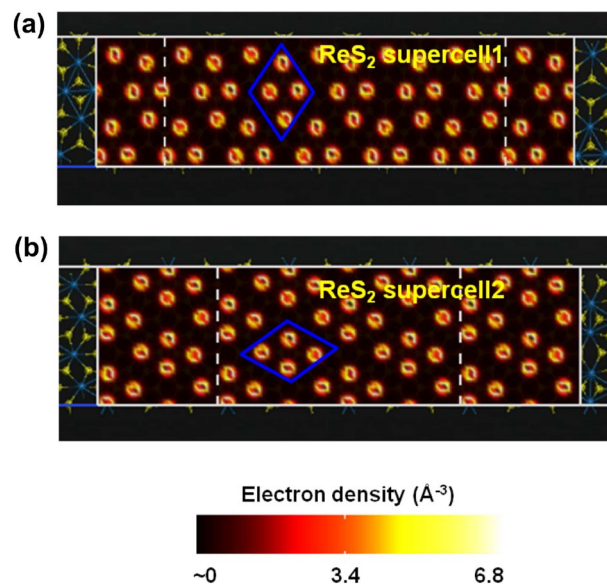
Figure 8. Electron density plots depicting the distribution of valence electrons around 'Re' atoms of ReS$_2$ supercell1 and ReS$_2$ supercell2.
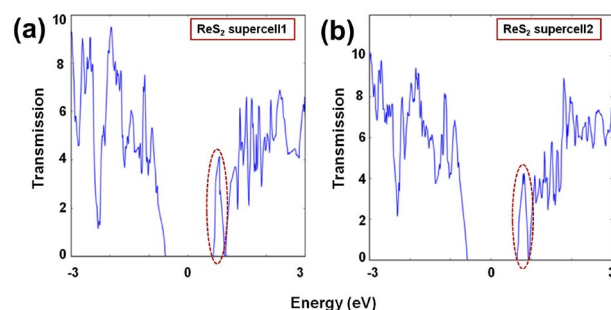
Figure 9. Transmission spectra (zero bias) of the two-port devices with (**a**) ReS$_2$ supercell1 and (**b**) ReS$_2$ supercell2 channel regions.

supercell2' . It is important to realize here that we have purposefully designed those supercell structures where the 'Re'-'Re' bonds are either parallel or perpendicular to the transport direction (Z direction). However, for single layer distorted 1T ReS$_2$, intrinsically the DS 'Re' chains form a certain angle with the [100]/[010] axis[20,29]. Thus, as illustrated in Fig. 10a, ReS$_2$ supercell3' (channel length = 4.620 nm and width = 1.143 nm) essentially exhibits the natural orientation of DS 'Re' chains.

Electron density plots of Fig. 8 depict how the valence electrons around 'Re' atoms are distributed across the channel regions. Apart from that, significant reduction in energy gap values can be observed for 'ReS$_2$ supercell1' and 'ReS$_2$ supercell2' (Fig. 9), owing to the large transmission states within the gap. Considering the transmission spectra as shown in Fig. 9, distinguishable transmission states within the range of 0.636 eV and 0.920 eV for 'ReS$_2$ supercell1' and 0.637 eV and 0.922 eV for 'ReS$_2$ supercell2', lower the energy gap values ($\sim$ 1.23 eV) of both the supercells.

However, the calculated energy gap for 'ReS$_2$ supercell3' (Fig. 10b) is $\sim$ 1.37 eV. More importantly, this value is similar to the bandgap of distorted 1T ReS$_2$ unit cell[20]. It further reinforces that the 'ReS$_2$ supercell3' has the geometry where orientation of DS 'Re' chains as well as distribution of valence electrons around 'Re' atoms (Fig. 10a), reflects that of the natural single layer.

Conclusion

In this work, electronic transmission in single layer distorted 1T ReS$_2$ and distorted 1T ReS$_2$ based type-II vdW heterointerfaces are studied. We have demonstrated that the ReS$_2$/MoSe$_2$ heterostructure exhibits stronger effect of interlayer coupling at the heterointerface, owing to the larger average value of charge re-distribution between the constituent layers. Moreover, we have compared the electronic transmission through ReS$_2$/WSe$_2$ and ReS$_2$/MoSe$_2$ channels, and computed their near-equilibrium conductance values. We have found that the ReS$_2$/MoSe$_2$ channel is more conducive to the charge carrier transport. Apart from that, we have explored the
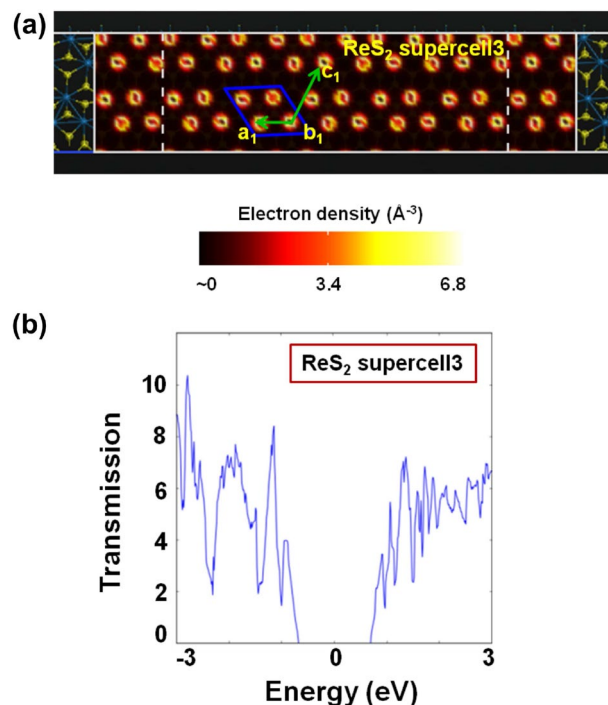
Figure 10. Plots illustrating the (**a**) electron density distribution around 'Re' atoms of ReS$_2$ supercell3 and (**b**) zero bias electronic transmission in two-port devices with ReS$_2$ supercell3 channel.

in-plane anisotropy of the group-7 constituent material, that is the single layer distorted 1T ReS$_2$ and investigated the role of clusterized 'Re' atoms in electronic transmission. This study may further be extended for fewlayer ReS$_2$/WSe$_2$ and ReS$_2$/MoSe$_2$ channels, to explore their electronic properties and compare the near-equilibrium conductance values.

Data availability

All relevant data that support the findings of this study are available from the corresponding author upon request.

References

1. Koppens, F. H. L. *et al.* Photodetectors based on graphene, other two-dimensional materials and hybrid systems. *Nat. Nanotechnol.* **9**, 780–793 (2014).
2. Berkelbach, Timothy C. & Reichman, David R. Optical and excitonic properties of atomically thin transition-metal dichalcogenides. *Ann. Rev. Condens. Matter Phys.* **9**, 379–396 (2018).
3. The International Technology Roadmap For Semiconductors 2.0., "Outside System Connectivity," 2015.
4. Lopez-Sanchez, Oriol, Lembke, Dominik, Kayci, Metin, Radenovic, Aleksandra & Kis, Andras. Ultrasensitive photodetectors based on monolayer MoS$_2$. *Nat. Nanotechnol.* **8**, 497–501 (2013).
5. Thorsten Deilmann and Kristian Sommer Thygesen. Dark excitations in monolayer transition metal dichalcogenides. *Phys. Rev. B* **96**, 201113(R) (2017).
6. Thakar, Kartikey *et al.* Multilayer ReS$_2$ photodetectors with gate tunability for high responsivity and high-speed applications. *ACS Appl. Mater. Interfaces* **10**(42), 36512–36522 (2018).
7. Ghosh, Sayantan, Varghese, Abin, Thakar, Kartikey, Dhara, Sushovan & Lodha, Saurabh. Enhanced responsivity and detectivity of fast WSe$_2$ phototransistor using electrostatically tunable in-plane lateral p-n homojunction. *Nat. Commun.* **12**, 3336 (2021).
8. Geim, A. K. & Grigorieva, I. V. Van der Waals heterostructures. *Nature* **499**, 419–425 (2013).
9. Lee, C.-H. *et al.* Atomically thin p-n junctions with van der Waals heterointerfaces. *Nat. Nanotechnol.* **9**, 676–681. https://doi.org/10.1038/NNANO.2014.150 (2014).
10. Furchi, M. M., Pospischil, A., Libisch, F., Burgdörfer, J. & Mueller, T. Photovoltaic effect in an electrically tunable van der waals heterojunction. *Nano Lett.* **14**, 4785–4791. https://doi.org/10.1021/nl501962c (2014).
11. Pulickel, A., Philip, K. & Kaustav, B. Two-dimensional van der Waals materials. *Phys. Today* **69**(9), 38 (2016).
12. Long, Y. *et al.* Photocarrier generation from interlayer charge-transfer transitions in WS$_2$-graphene heterostructures. *Sci. Adv.* **4**(2), e1700324 (2018).
13. Chenhao, J. *et al.* Ultrafast dynamics in van der Waals heterostructures. *Nat. Nanotechnol.* **13**, 994–1003 (2018).
14. Wang, Zilong *et al.* Phonon-mediated interlayer charge separation and recombination in a MoSe$_2$/WSe$_2$ heterostructure. *Nano Lett.* **21**(5), 2165–2173 (2021).
15. Xia, Fengnian, Mueller, Thomas, Lin, Yu.-ming, Valdes-Garcia, Alberto & Avouris, Phaedon. Ultrafast graphene photodetector. *Nat. Nanotechnol.* **4**, 839–843 (2009).
16. Guo, Qiushi *et al.* Black phosphorus mid-infrared photodetectors with high gain. *Nano Lett.* **16**(7), 4648–4655 (2016).
17. Massicotte, Mathieu *et al.* Dissociation of two-dimensional excitons in monolayer WSe$_2$. *Nat. Commun.* **9**, 1633 (2018).

18. Alamri, Mohammed, Gong, Maogang, Cook, Brent, Goul, Ryan & Wu, Judy Z. Plasmonic WS_2 nanodiscs/graphene van der waals heterostructure photodetectors. *ACS Appl. Mater. Interfaces* **11**(36), 33390–33398 (2019).
19. Chulho, P. *et al.* Photovoltaic effect in a few-layer ReS_2/WSe_2 heterostructure. *Nanoscale* **10**, 20306 (2018).
20. Saha, Dipankar, Varghese, Abin & Lodha, Saurabh. Atomistic modeling of van der Waals Heterostructures with Group-6 and Group-7 monolayer transition metal dichalcogenides for near infrared/short-wave infrared photodetection. *ACS Appl. Nano Mater.* **3**, 820–829 (2020).
21. Pranjal, K. G. *et al.* Layer rotation-angle-dependent excitonic absorption in van der waals heterostructures revealed by electron energy loss spectroscopy. *ACS Nano* **13**(8), 9541–9550 (2019).
22. Varghese, Abin *et al.* Near-direct bandgap WSe_2/ReS_2 Type-II pn heterojunction for enhanced ultrafast photodetection and high-performance photovoltaics. *Nano Lett.* **20**(3), 1707–1717 (2020).
23. Hyun, S. L. *et al.* Tunneling photocurrent assisted by interlayer excitons in staggered van der waals hetero-bilayers. *Adv. Mater.* **29**, 1701512 (2017).
24. Li, Ning *et al.* SWIR photodetection and visualization realized by incorporating an organic SWIR sensitive bulk heterojunction. *Adv. Sci.* **7**, 2000444 (2020).
25. Chulyeon, L., Hwajeong, K., Youngkyoo, K., Short-wave infrared organic phototransistors with strong infrared-absorbing poly-triarylamine by electron-transfer doping. *NPJ Flexible Electron.*, p. 10, (2021).
26. Dipankar, S. & Saurabh, L. Study of transmission properties of distorted 1T ReS_2 based type-II van der Waals heterostructures. *MRS Fall Meet.*, (2020).
27. Arup Kumar, P. *et al.* Photo-tunable transfer characteristics in $MoTe_2$-MoS_2 vertical heterostructure. *NPJ 2D Mater. Appl.*, 17 (2017).
28. Saha, Dipankar & Mahapatra, Santanu. Anisotropic transport in 1T′ monolayer MoS_2 and its metal interfaces. *Phys. Chem. Chem. Phys.* **19**, 10453–10461 (2017).
29. Lin, Yung-Chang. *et al.* Single-layer ReS_2: Two-dimensional semiconductor with tunable in-plane anisotropy. *ACS Nano* **9**(11), 11249–11257 (2015).
30. Chenet, Daniel A. *et al.* In-plane anisotropy in mono- and few-layer ReS_2 probed by raman spectroscopy and scanning transmission electron microscopy. *Nano Lett.* **15**, 5667–5672 (2015).
31. Jang, Hyejin, Ryder, Christopher R., Wood, Joshua D., Hersam, Mark C. & Cahill, David G. 3D anisotropic thermal conductivity of exfoliated rhenium disulfide. *Adv. Mater.* **29**, 1700650 (2017).
32. Goyal, Natasha, Parihar, Narendra, Jawa, Himani, Mahapatra, Souvik & Lodha, Saurabh. Accurate threshold voltage reliability evaluation of thin Al_2O_3 top-gated dielectric black phosphorous FETs using ultrafast measurement pulses. *ACS Appl. Mater. Interfaces* **11**(26), 23673–23680 (2019).
33. Rahman, Mohammad, Davey, Kenneth & Qiao, Shi-Zhang. Advent of 2D rhenium disulfide (ReS_2): Fundamentals to applications. *Adv. Funct. Mater* **27**, 1606129 (2017).
34. Manish, C., Hyeon, S.S., Goki, E., Lain-Jong, L., Kian, P.L., Hua, Z., The chemistry of two-dimensional layered transition metal dichalcogenide nanosheets. *Nat. Chem.*, vol. 5, (2013).
35. QuantumATK version 2018.06, Synopsys QuantumATK. Available at https://www.synopsys.com/silicon/quantumatk.html.
36. Smidstrup, Søren. *et al.* QuantumATK: An integrated platform of electronic and atomic-scale modelling tools. *J. Phys. Condens. Matter* **32**, 015901 (2020).
37. Perdew, J. P., Burke, K. & Ernzerhof, M. Generalized gradient approximation made simple. *Phys. Rev. Lett.* **77**(18), 3865–3868. https://doi.org/10.1103/PhysRevLett.77.3865 (1996).
38. Ozaki, T. Variationally optimized atomic orbitals for large-scale electronic structures. *Phys. Rev. B* **67**, 155108. https://doi.org/10.1103/PhysRevB.67.155108 (2003).
39. Ozaki, T. & Kino, H. Numerical atomic basis orbitals from H to Kr. *Phys. Rev. B* **69**, 195113. https://doi.org/10.1103/PhysRevB.69.195113 (2004).
40. Grimme, S. Semiempirical GGA-type density functional constructed with a long-range dispersion correction. *J. Comput. Chem.* **27**(15), 1787–1799 (2006).
41. Tong, Zhen, Dumitrica, Traian & Frauenheim, Thomas. First-principles prediction of infrared phonon and dielectric function in biaxial hyperbolic van der Waals crystal α-MoO_3. *Phys. Chem. Chem. Phys.* **23**, 19627–19635 (2021).
42. Markussen, T., Jauho, A.-P. & Brandbyge, M. Electron and phonon transport in silicon nanowires: Atomistic approach to thermoelectric properties. *Phys. Rev. B* **79**, 035415 (2009).
43. Saha, D. & Mahapatra, S. Theoretical insights on the electro-thermal transport properties of monolayer MoS_2 with line defects. *J. Appl. Phys.* **119**, 134304. https://doi.org/10.1063/1.4945582 (2016).
44. Brandbyge, M., Mozos, J.-L., Ordejón, P., Taylor, J. & Stokbro, K. Density-functional method for nonequilibrium electron transport. *Phys. Rev. B* **65**, 165401. https://doi.org/10.1103/PhysRevB.65.165401 (2002).
45. Wyckoff, R. W. G., Crystal structures. p. 1, (1963).
46. Schutte, W. J., De Boer, J. L. & Jellinek, F. Crystal structures of tungsten disulfide and diselenide. *J. Solid State Chem.* **70**(2), 207–209 (1987).
47. Kristin, P. Materials data on ReS_2 (SG:2) by materials project. United States. https://doi.org/10.17188/1276430
48. Shi, Zhiming, Wang, Xinjiang, Sun, Yuanhui, Li, Yawen & Zhang, Lijun. Interlayer coupling in two-dimensional semiconductor materials. *Semicond. Sci. Technol.* **33**, 093001 (2018).

Acknowledgements

Author contributions

D.S. and S.L. conceived the idea of this work. D.S. carried out the atomistic modeling of vdW heterostructures. D.S. performed the theoretical study employing DFT-NEGF combination and analysed the results. S.L. supervised the work. D.S. and S.L. wrote the manuscript.

Competing interests

The authors declare no competing interests.

Additional information

Supplementary Information The online version contains supplementary material available at https://doi.org/10.1038/s41598-021-02704-2.

Correspondence and requests for materials should be addressed to D.S.

Reprints and permissions information is available at www.nature.com/reprints.

Publisher's note Springer Nature remains neutral with regard to jurisdictional claims in published maps and institutional affiliations.